Monitoring of Thermal Processes for Medical Applications Using Infrared Thermography

By

Shan Lin

Thesis

Submitted to the Faculty of the

Graduate School of Vanderbilt University

in partial fulfillment of the requirements

for the degree of

MASTER OF SCIENCE

in

Electrical Engineering

May, 2017

Nashville, Tennessee

Approved:

Robert J. Webster III, Ph.D.

Greg Walker, Ph.D.

To my parents.

ACKNOWLEDGMENTS

I would first like to thank my advisor Dr. Robert J. Webster III. He gave many unique and meaningful guidances for my research and future academic career. I would also like to thank Dr. Loris Fichera. He spent much of his valuable time talking through professional skills, experience and reviewing drafts of my thesis. My appreciation also goes out to Trevor L. Bruns for his assistance in the construction of the stereocamera system. I would also like to acknowledge Neal P. Dillon and Mitchell J. Fulton for their work in the bone drilling experiment for cochlear implantation.

TABLE OF CONTENTS

Page

DEDICATION ii

ACKNOWLEDGMENTS iii

LIST OF FIGURES vi

Chapter

1 INTRODUCTION 1

1.1 Temperature Monitoring Methods for Surgery 2

1.2 Scope of the Thesis 3

1.3 Thesis Overview 4

2 FUNDAMENTALS OF INFRARED THERMAL CAMERA TECHNOLOGY AND APPLICATIONS IN MEDICINE 5

2.1 Infrared (IR) Thermography Theory 5

2.2 Thermal Camera Technology 7

2.3 Applications of Thermography in Medicine 8

2.3.1 Thermoregulation Studies 10

2.3.2 Detection of Breast Cancer 10

2.3.3 Temperature Monitoring of Heat-Based Medical Treatment 10

2.3.4 Mass Fever Screening 11

2.4 Towards IR-Based Thermal Monitoring for Surgical Applications 11

2.4.1 FLIR A655sc 11

2.4.2 FLIR Lepton 12

3 IR CAMERA-BASED MONITORING OF BONE DRILLING 13

3.1 Background: Minimally-Invasive Cochlear Implantation 13

3.2 Experimental Setup 14

3.3 Thermal Video Acquisition 16
3.4 Clock Synchonization Algorithm 18
3.5 Discussion 20
4 THERMAL MONITORING OF VESSEL SEALING USING A MINIATURE INFRARED CAMERA 21
4.1 Thermal Stereocamera System 21
4.1.1 Temperature Calibration 22
4.1.2 Optical Stereo Calibration 24
4.2 Experimental Validation 25
4.2.1 Temperature Estimation 26
4.2.2 Spatial Extent of Thermal Spread 27
4.3 Discussion 28
5 CONCLUSIONS AND FUTURE OUTLOOK 30
BIBLIOGRAPHY 31

LIST OF FIGURES

Figure Page

1.1 Example of tissue carbonization caused by surgical laser 2

2.1 The spectral radiance of blackbody radiation at different temperatures 7
2.2 Example of cavity type commercial blackbody 9
2.3 Example of hot plate type commercial blackbody 9
2.4 Commercial IR thermal cameras used in this thesis 12

3.1 Cochlear implant 13
3.2 Preoperative drill path planning for minimaly-invasive cochlear implantation 15
3.3 Experimental setup to study temperature elevation of temporal bone created by the drill 15
3.4 The block diagram of the experiment system 16
3.5 Example of synchronized thermal data and drill position advancement 19

4.1 Thermal stereocamera system based on the FLIR Lepton 21
4.2 Temperature calibration 23
4.3 Thermal stereocamera calibration 24
4.4 Example of 3D reconstruction of the checkerboard after stereo calibration . . 25
4.5 Experimental validation of the thermal stereocamera 27
4.6 Mean and peak temperature created by the cautery pen on the surface of tissue 28

Chapter 1

INTRODUCTION

Surgical interventions frequently involve the use of instruments that apply heat to tissue. Cauterization is one example: this refers to the practice of coagulating blood vessels by rapidly heating up tissue, with the aim of controlling bleeding and maintaining good visibility of the surgical scenario. Coagulation occurs when the temperature of tissue is elevated between 45°C and 60°C [1, 2] and can be achieved with a variety of tools, including electric probes, lasers and ultrasonic forceps [1, 3].

Controlling the elevation of tissue temperature during a surgical intervention is vital to a successful surgical outcome. This is particularly important when operating in proximity to delicate anatomy, where the buildup of temperature can cause accidental tissue damage and result in adverse effects. Nerve damage secondary to heat is a common complication of prostatectomy [4], and is associated with permanent erectile dysfunction and urinary incontinence [5]. Nerves are known to be particularly sensitive to temperature increase, with temperatures as low as 45°C already posing a significant risk of injury [6]. Another important type of thermal tissue damage is carbonization (also referred to as charring in the medical literature); this occurs when the temperature rises above 100°C and is a severe type of tissue necrosis [7]. Carbonization is commonly observed in laser surgery, as it is often the result of an erroneous selection of laser parameters, e.g. prolonged laser exposure [8]. An example of carbonization is shown in Fig. 1.1, which shows tissue that was treated with a surgical laser and carbonized as a result of excessive heat. From a clinical standpoint, carbonization - and more generally any kind of thermal tissue damage - should be avoided because it results in longer healing times and may leave scars [7].

To limit the extent of thermal tissue damage, it would be necessary to control the heat generation and spread to surrounding tissue. Prior research in the medical field has eval-

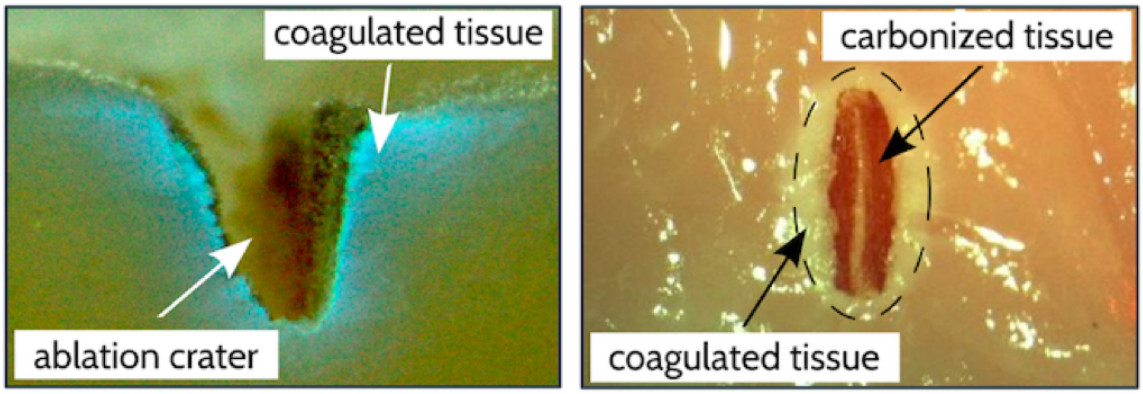

Figure 1.1: Example of tissue carbonization caused by surgical laser.

uated the heat spread of different cautery instruments [9, 3, 10], and the findings have stimulated the development of novel solutions to reduce such spread [11, 12, 13, 14]. Despite these technological advancements, recent studies suggest that the use of heat-based instruments in surgery still represents a significant challenge to many clinicians, particularly due to the lack of intraoperative temperature feedback [14, 15]. We hypothesize that if surgeons had access to thermal information during surgery, this would facilitate their understanding of thermal processes occurring at the surgical site and enhance the control of such processes, e.g. they could interrupt tissue cauterization if tissue overheating is detected. Building on this hypothesis, the work described in this thesis lays the groundwork for the development of novel methods to monitor and control tissue temperature during surgical interventions.

1.1 Temperature Monitoring Methods for Surgery

The development of methods to monitor the temperature of tissue during a medical procedure is a vast field of study, and a survey of existing methods was recently provided by Saccomandi et al. [16]. Briefly, these methods can be divided into three categories. Invasive approaches use sensors in close proximity to the surgical site. These sensors are generally simple to use and cost-effective; however, they only enable point measurement and are thus ineffective in applications where the monitoring of a large area of tissue is

needed. Furthermore, they require the introduction of sensing equipment in proximity to the surgical site, something that may be impractical in many surgeries. In order to overcome these disadvantages, alternative, non-invasive techniques based on medical imaging technologies, such as Computed Tomography (CT), Magnetic Resonance Imaging (MRI) and ultrasound imaging, are being developed [16]. These methods work by mapping changes in tissue appearance to temperature variations. In contrast to invasive methods, image-based thermometry does not require the introduction of additional instruments or probes in the surgical site. These techniques may require significant alterations in the procedure workflow (e.g. the use of MRI-compatible equipment), and involve exposure to radiation (in the case of CT). The third and last class of monitoring methods involves the use of mathematical models to predict the temperature of tissue created by a specific instrument [17]. These models are calculated by solving the direct heat conduction problem in tissue, assuming given initial and boundary conditions.

In contrast to existing approaches, we propose to use Infrared (IR) thermal imaging as a method to monitor the temperature of tissue in a surgical intervention. Until now, the application of this technology to surgery has been limited by (1) the large size of thermal imaging systems, which has made their integration in a surgical setting impractical; and (2), the lack of software to effectively integrate thermal cameras with other sensing equipment used in the operating room. As we shall see in the next section, the work presented in this thesis tackles both of these issues and lays the groundwork for future use of IR thermal imaging not just in surgery, but in a variety of different medical applications.

1.2 Scope of the Thesis

This thesis presents technical contributions aimed to enable IR imaging-based monitoring of tissue temperature in two specific scenarios:

- **Benchtop Bone Drilling Experiments** A MATLAB script was developed to enable the integration of an IR thermal camera in a benchtop experimental setup aimed at

studying the thermal effects of bone drilling. The script utilizes the GiGE vision protocol to communicate with the camera and acquire a stream of thermal images. A clock synchronization algorithm is implemented to enable the synchronization between the timestamps of thermal images and events recorded by other sensing instruments in the experimental setup.

- **Thermal Coagulation of Soft Tissue** A thermal stereocamera system was created to enable the monitoring of thermal processes during minimally-invasive surgery, e.g. the coagulation of blood vessels with a cautery instrument. The system consists of two miniature thermal cameras that were recently launched on the market. Here we present procedures to perform the temperature and optical calibration of the two cameras, and conduct experiments to validate the output of the stereocamera system.

1.3 Thesis Overview

The remainder of this thesis is outlined as follows: Chapter 2 reviews the fundamentals of IR thermal imaging and provides a review of prior applications of this technology in the medical field. Chapter 3 presents the MATLAB software developed for the benchtop bone drilling experiments. The chapter further provides context on the specific surgical application for which these experiments were designed, i.e. minimally-invasive cochlear implantation. Chapter 4 presents the thermal stereocamera system aimed to enable thermal monitoring in minimally-invasive surgery. Finally, Chapter 5 outlines the conclusions of this thesis and discusses future work.

Chapter 2

FUNDAMENTALS OF INFRARED THERMAL CAMERA TECHNOLOGY AND APPLICATIONS IN MEDICINE

This chapter reviews the fundamentals of infrared (IR) camera technology. The concepts presented here constitute the foundation of the work presented in this thesis. We first review the fundamental physical principles of infrared thermography, and then provide a brief overview of how IR cameras are calibrated. We then provide a survey of existing applications of IR thermography in medicine. The Chapter is concluded by an overview of the IR camera systems used throughout this thesis.

2.1 Infrared (IR) Thermography Theory

Infrared (IR) thermography, also commonly known as thermal imaging, denotes a temperature estimation technique based on the measurement of the amount of IR radiation emitted by an object. In general, every physical object continuously emits electromagnetic (EM) radiation [18], and the relation between the radiated power and the corresponding temperature T is described by the Stefan-Boltzmann law [19]

$$P = \sigma T^4, \tag{2.1}$$

where P is the energy radiated per unit area (W/m^2), and σ is the Stefan-Boltzmann constant, i.e. $\sigma = 5.67 \times 10^{-8}\ W \cdot m^{-2} \cdot K^{-4}$. Eq. (2.1) establishes that the amount of energy emitted by an object under the form of EM radiation is directly proportional to the fourth power of its temperature. It is important to note that this relation applies to the ideal case of a *blackbody*. By definition, a blackbody is an idealized physical object that emits more EM radiation than any other non-ideal object at the same temperature. The EM emission of a blackbody is described by Planck's law, as we shall see later in this section. Objects in

the physical world generally emit radiation at a fraction of that of a blackbody. To account for this phenomenon, Eq. 2.1 can be rewritten as [20]

$$P = \varepsilon \sigma T^4, \tag{2.2}$$

where ε is defined as the *emissivity* of the object. Emissivity is a real number between 0 and 1 and depends on the specific type of material. By definition, a blackbody has a perfect emissivity, i.e. $\varepsilon = 1$. Metals generally present a low emissivity, e.g. the emissivity of aluminum is reported to be 0.05-0.07 [21], while high-emissivity materials include water (0.98 [21]) and human skin (0.98 [22]).

The spectral emission of a blackbody is described by Planck's law [19]

$$L_\lambda(T) = \frac{2hc^2}{\lambda^5} \frac{1}{e^{\frac{hc}{\lambda k_B T}} - 1}, \tag{2.3}$$

where λ denotes the wavelength, L_λ is the spectral radiance per unit wavelength λ ($W \cdot sr^{-1} \cdot m^{-3}$), h is the Planck constant ($h = 6.63 \times 10^{-34}\ J \cdot s$), k_B is the Boltzmann constant ($k_B = 1.38 \times 10^{-23}\ J \cdot K^{-1}$), and c is the speed of EM radiation in vacuum ($c = 3.00 \times 10^8 m/s$). The plot in Fig. 2.1 shows Planck's curves for different values of temperature.

Eqs. 2.1 and 2.3 constitute the basic physical principles of infrared thermometry. In particular, Eq. 2.1 establishes that by measuring the radiation intensity emitted by an object, it is possible to estimate its temperature; Eq. 2.3 models the relation between the object temperature and the spectral distribution of emitted intensity. It can be observed that for temperatures below 500°C, much of the emission is concentrated in the infrared range of wavelengths. In particular, the radiance peaks are at approximately $10 \mu m$ when the object is at room temperature (20°C and 25°C [23]). Many commercial infrared thermometers are sensitive to radiation in the 7-14 μm range, as we shall see later in this Chapter.

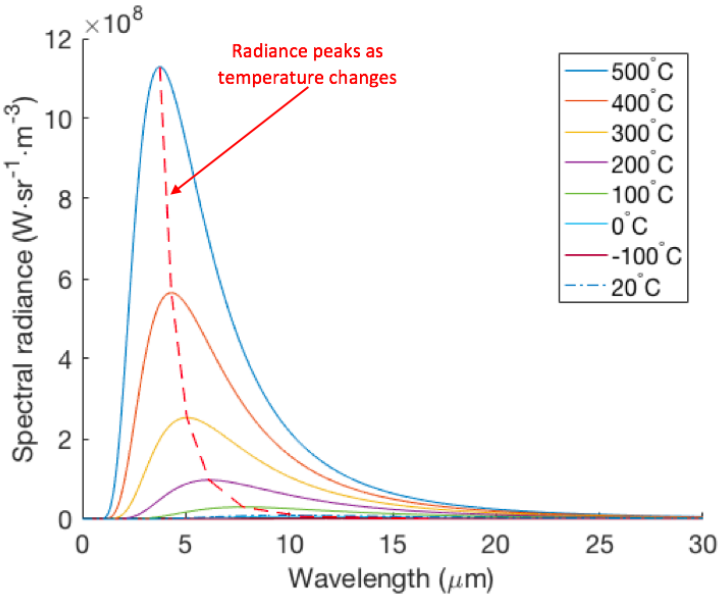

Figure 2.1: The spectral radiance of blackbody radiation at different temperatures.

2.2 Thermal Camera Technology

Having reviewed the fundamental physical principles that enable IR thermometry, in this section we focus on IR thermal cameras and briefly review their operational principles. For a comprehensive resource on thermal camera technology, the reader is referred to [19, 24].

The imaging sensor of a thermal camera consists of an array of elemental detectors, which measure the IR radiation intensity emitted by an object. Each elemental detector corresponds to a pixel in the thermal images produced by the camera. The relation between the raw pixel output P and the temperature T of the target object can be approximated using Planck's curve [24]

$$P = \frac{R}{e^{\frac{B}{T}} - F} + O \tag{2.4}$$

with R, B, F and O being coefficients that are estimated through a calibration procedure, as

described later in this section. The inverse function of Eq. 2.4 is

$$T = \frac{B}{ln(\frac{R}{P-O} + F)}, \tag{2.5}$$

which can be used to estimate the temperature based on the camera's raw output. Non-linear regression is commonly used to estimate the coefficients in this model. In principle, each individual pixel should be calibrated separately, i.e. each elemental detector on the thermal imaging sensor presents its own calibration curve. Data for the calibration is obtained by exposing the camera sensor to known reference temperatures and measuring the raw output of each pixel.

The devices typically used in thermal camera calibration are blackbodies, which are approximations of the ideal blackbody. A surrogate blackbody generally presents two important characteristics: (1) it absorbs most of the incident environmental IR radiation that would otherwise be detected by the camera and create noise, hindering the calibration procedure; (2) it should present a strong emission, i.e. as close as possible to ideal value of $\varepsilon = 1.0$. One commonly used approach to create blackbodies consists in making a temperature-controlled dark cavity, as shown in Fig. 2.4 [25]. Hot plates made of high-emissivity materials (as in Fig 2.3) are another common type of blackbody used for thermal camera calibration.

2.3 Applications of Thermography in Medicine

In the past, numerous studies have explored the use of IR thermography for medical applications. From a clinical perspective, this technology is appealing because it enables a simple, non-contact and relatively inexpensive method to monitor the temperature of the human body and possibly detect abnormal physiological processes [28]. In this section, we review some of the most relevant applications of IR thermography to medicine. For a comprehensive review of such applications, the reader is referred to [29].

(a) Calibration Source M300.

(b) Schematic diagram.

Figure 2.2: Example of cavity type commercial blackbody [26]. (a) shows an example of commercial blackbody cavity for infrared thermometer calibration (Calibration Source M300, by LumaSense Technologies, Inc.). (b) shows the cross-section of a cavity-based blackbody. A thermocouple is used to control the internal temperature of the cavity.

Figure 2.3: Example of hot plate type commercial blackbody (Surface Hot Plate CBB15GC, by Palmer Wahl Instrumentation Group) [27]. The temperature of the hot plate is controllable.

2.3.1 Thermoregulation Studies

Thermoregulation denotes the set of physiological mechanisms by which the human body self-regulates its temperature. Typical examples include heat perfusion through the blood stream and sweating, i.e. heat exchange with the environment. Understanding and monitoring these mechanisms is important, as they are suspected to reflect the overall health condition of a human being and potentially enable the detection of underlying disease processes. Prior research in this area include use of IR cameras to monitor the external surface of the body to study the dynamics of peripheral blood flow [30], the relation between diabetes and temperature in feet and hands [31, 32, 33], as well as cutaneous perspiration [34].

2.3.2 Detection of Breast Cancer

Prior research suggests that thermal imaging could be used to provide early diagnosis of breast cancer [35, 36, 37, 38]. Compared to other conventional diagnosis methodologies such as mammography, IR thermography presents the advantage of not involving exposure to ionizing radiation. Despite this advantage, the effectiveness of this diagnostic method is still not widely accepted and a subject of debate [32, 33]. As of today, the Food and Drug Administration (FDA) recommends the use of thermal imaging for breast cancer detection only as an adjunctive diagnostic method [39].

2.3.3 Temperature Monitoring of Heat-Based Medical Treatment

Several medical treatment modalities involve the use of energy based instruments to artificially increase the temperature of tissue. Improper use of these instruments might lead to thermal injury. Prior research has explored the use of IR thermography to mitigate such a risk. In particular, Thomas et al. reported the use of thermal images for optimal laser parameter setting during laser skin treatment especially for vascular lesions and depilation [40]. Cummings et al. highlighted the potential application of thermography in dental surgery for heat spread monitoring of electro-thermal debonding (ETD), which is a process

to remove a bracket from a tooth [41]. It can also be used to investigate heat spread pattern during dental bone drilling [42].

2.3.4 Mass Fever Screening

IR thermal cameras are routinely used at airports and other majors transportation hubs to detect and quarantine travelers affected by pandemic diseases, e.g. influenza [43, 44, 45]. The advantage of IR thermography for this application is that it enables an instantaneous, non-contact measurement of body temperature [46, 47].

2.4 Towards IR-Based Thermal Monitoring for Surgical Applications

As we have seen in the previous section, until now, applications of IR thermography to medicine have been limited to observing the external surface of the body. This can be partially attributed to the size of thermal camera systems, that are traditionally large and therefore not amenable to monitor thermal processes occurring inside the human body, e.g. during a surgical intervention. Another important roadblock is the lack of software to integrate IR cameras with other sensors, thereby making it difficult to correlate thermal information with observed events. The work presented in this thesis aims to overcome these limitations and lay the groundwork for future applications of IR camera technology inside the human body. Our investigation involved the use of two commercial IR thermal camera systems, as outlined below.

2.4.1 FLIR A655sc

The FLIR A655sc (FLIR Systems, Inc., CA; see Fig. 2.4a) is a Long-Wave IR (LWIR) camera and detects EM radiation that lies in long-wavelength infrared (wavelengths: 7.5-14μm). The A655sc has a resolution of 640×480 and a frame rate of up to 200 Hz [48]. This camera has temperature resolution of 10mK. It is factory calibrated for temperature measurement in the range between -40°C and 150°C and between 100°C and 650°C. The

(a) FLIR A655sc [48].

(b) FLIR Lepton [49].

Figure 2.4: Commercial IR thermal cameras used in this thesis.

A655sc offers two digital interfaces namely USB and GiGE. The latter is a standard interface for industrial cameras [50].

2.4.2 FLIR Lepton

The other IR thermal camera used in our work is the FLIR Lepton (FLIR Systems, Inc., CA; see Fig. 2.4b) [51]. With a footprint of 8.5x11.7x5.6 mm, the FLIR Lepton is the smallest IR thermal detector commercially-available to date, and was originally designed for integration with mobile devices and other consumer electronics such as mobile phones. Like the A655sc, the Lepton is sensitive to incident radiation in the long infrared range (wavelengths: 8-14μm). The imaging detector has a resolution of 60x80 pixels, with a field of view of 50° and a frame rate of 9 fps.

Unlike the A655sc, the Lepton does not provide absolute temperature measurements, i.e. the device is not factory-calibrated. Thus, in order to use this camera for thermal monitoring, the calibration procedure described earlier in section 2.2 must be performed.

Chapter 3

IR CAMERA-BASED MONITORING OF BONE DRILLING

In this Chapter we present an experimental setup aimed to study the temperature elevation of bone during surgical drilling. We will focus on a specific surgical scenario, i.e. bone drilling for minimally-invasive cochlear implantation. The experimental setup involves the use of a IR thermal camera to measure the temperature of bone throughout the experiments. Here we present a MATLAB script that streamlines the acquisition of the video stream produced by the camera.

3.1 Background: Minimally-Invasive Cochlear Implantation

A cochlear implant is an electronic device that restores hearing to individuals with severe hearing loss [52]. Fig. 3.1 illustrates the different components of a cochlear implant: a microphone picks up sounds from the environment and transmits them to a receiver which is surgically implanted on the patient. The terminal part of the receiver, i.e. the electrode (refer to Fig. 3.1a) is threaded into the cochlea, which is located deep into the ear. Once the device is implanted and turned on, electric signals will stimulate the cochlea, recreating the perception of sound.

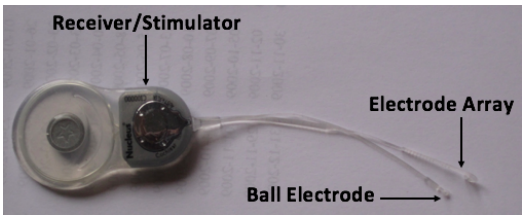

(a) The internal part of a cochlear implant [53].

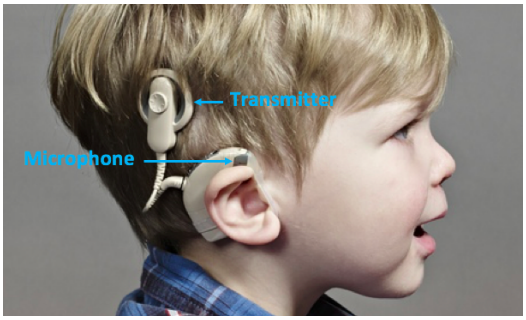

(b) The external part of a cochlear implant [54].

Figure 3.1: Cochlear implant.

Cochlear implant surgery is normally an invasive surgical intervention which requires the removal of a large volume of bone from the skull to enable access to the internal structures of the ear [55]. To reduce the invasiveness of this process and cause less trauma on patients, a new approach - minimally-invasive image-guided cochlear implantation - has been proposed. Fig. 3.2 illustrates this approach: access to the cochlea is enabled by drilling a narrow tunnel from the external surface of the skull. The position and orientation of the tunnel is determined pre-operatively, based on CT imaging. One challenge with this approach is that the drilling path (yellow cylinder in Fig. 3.2) must be drilled in the proximity to vital anatomical structures that are embedded in the bone. Among others, these include the facial nerve, i.e. the nerve that controls facial muscles. In prior work, researchers have succeeded in making drilling for minimally-invasive cochlear implantation accurate enough to prevent accidental collisions with the facial nerve, and this has enabled the clinical translation of the procedure [55, 56]. Nonetheless, one major complication emerged during one of the early clinical trials, namely the facial nerve of one of the patients was thermally injured because of the heat generated by the drill bit [55]. This prompted researchers to investigate the drilling process and establish safeguards to reduce the amount of heat created during bone drilling. Our laboratory at Vanderbilt recently set up an experiment to quantify the temperature elevation of bone subject to drilling, using the same protocol described in [55]. The setup of this experiment is described in the next section.

3.2 Experimental Setup

Fig. 3.3 illustrates the setup of the experiment. A manual drill press, not unlike the one used during the early clinical trials [55], was used to drill access tunnels in cadaveric temporal bones. The temporal bone is that portion of the skull that contains the internal structures of the ear, including the cochlea. The goal of the experiment was to measure the temperature elevation created by the drill when passing closest to the facial nerve. CT

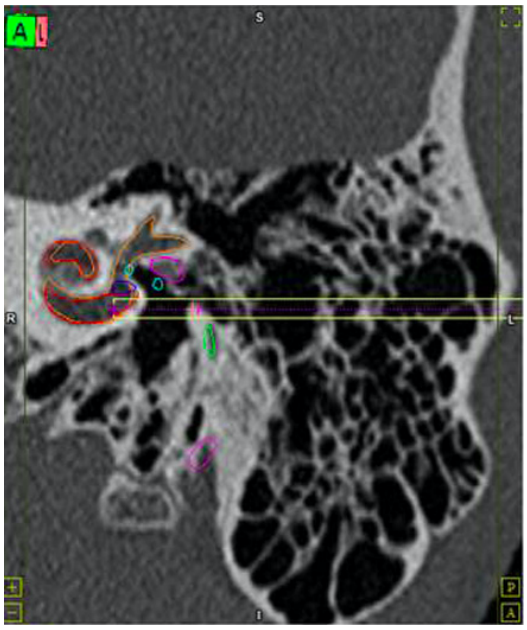

Figure 3.2: Preoperative drill path planning for minimaly-invasive cochlear implantation. Segmented anatomis include the scala tympani (red), scala vestibuli (blue), facial nerve (magenta), chorda tympani (green), ossicles (blue), and external auditory canal (yellow); the drill trajectory is shown as a yellow cylinder [55].

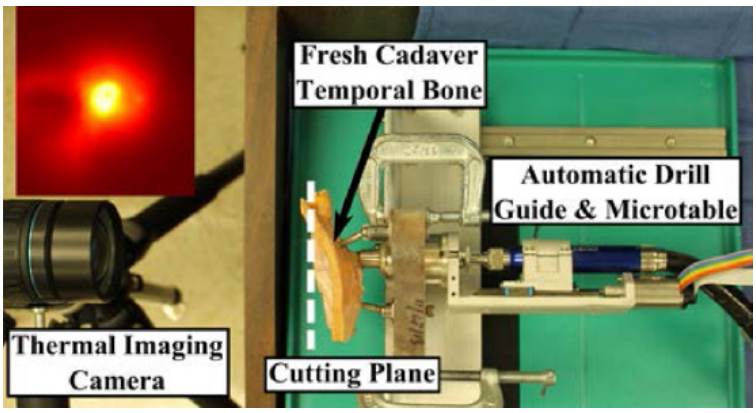

Figure 3.3: Experimental setup to study temperature elevation of temporal bone created by the drill [57]. The figure in the upper-left corner is an example of the thermal image captured by the thermal camera (FLIR A655sc).

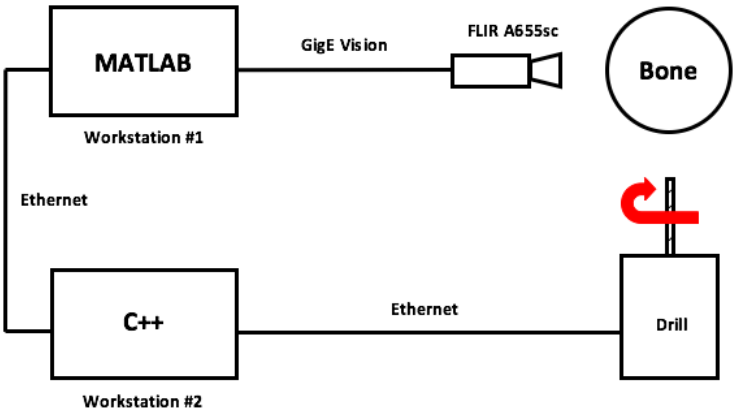

Figure 3.4: The block diagram of the experiment system.

imaging was used to determine the location of the facial nerve in the bone (Fig. 3.2) and identify the location where the drill path passes closest to it. The bone was subsequently cut to expose this location (refer to cutting plane in Fig 3.3) and an infrared thermal camera (FLIR A655sc) was used to monitor the temperature at this location throughout the experiment. Bone presents an emissivity of 0.96 [58], therefore an IR thermal camera can accurately estimate its temperature. To correlate the advancement of the drill with the thermal effects observed by the camera, the software system shown in Fig. 3.4 was developed. The camera was connected via Ethernet to an external workstation (#1), where a MATLAB script takes care of acquiring the stream of thermal images. Another workstation (#2) runs a C++ software that records the advancement of the drill press. To enable synchronization between the thermal video and drill position information, a distributed clock synchronization algorithm was implemented between the two workstations, as detailed later in this chapter.

3.3 Thermal Video Acquisition

This section describes the software implemented to capture thermal videos from the FLIR A655sc. The software was implemented in MATLAB and utilizes the Image Acquisition Toolbox [59] to establish a connection to the camera through the GigE protocol [50].

One of the advantages of implementing the acquisition software in MATLAB is the data is immediately available in the MATLAB workspace for analysis.

The code in listing 3.1 illustrates the structure of the acquisition software. First, a connection to the camera is established using the `videoinput` function (line 4) and specifying `gige` as connection parameter. Access to the camera internal settings can be retrieved via a call to the `getselectedsource` function. One important parameter that must be set is the format of the images provided by the camera. For these experiments it was set to `TemperatureLinear100mK`. When this setting is selected, the camera encodes images using an integer format. A unit variation in the value of a pixel represents a variation of +/-100 mK in the temperature of the object being observed. The instruction on Line 25 of listing 3.1 illustrates how to convert raw data to absolute temperature values.

Listing 3.1: MATLAB Script for Video Acquisition from the FLIR A655sc Camera

```
1  FRAMES2CAPTURE = 200;
2
3  %% Initialize connection to the camera
4  camera = videoinput('gige', 1, 'Mono16');
5  cam_conf = getselectedsource(camera);
6  cam_conf.IRFormat = 'TemperatureLinear100mK';
7  cam_conf.IRFrameRate = 'Rate25Hz';
8
9  %% Set number of frames to capture
10 %  Set FRAMES2CAPTURE = Inf at the beginning of the program
11 %  for continuous acquisition
12 camera.FramesPerTrigger = FRAMES2CAPTURE;
13
14 %% Record video
15 start(camera);
```

```
16
17 while(camera.FramesAcquired < FRAMES2CAPTURE)
18     continue;
19 end
20
21 stop(camera);
22 [frames, timestamps] = getdata(camera);
23
24 frames = single(frames);
25 frames = frames * 0.1 - 273.15;
26
27 %% Clean up and terminate
28 %  Set camera mode back to 'Radiometric'
29 cam_conf.IRFormat = 'Radiometric';
```

3.4 Clock Synchonization Algorithm

As mentioned earlier in section 3.2, the thermal video and drill advancement were recorded by two separate workstations. To synchronize these two data streams, a temporal synchronization procedure was implemented, based on the algorithm proposed in [60]. This algorithm, known in the computer science literature as Cristian's algorithm, estimates the offset between the clocks within a network of computers so to enable the creation of a common temporal reference.

The pseudocode of the temporal synchronization procedure is shown in listing 3.2. At the beginning of each drilling trial, W1 communicates its local time to W2. Upon reception of the message, W2 sets its local clock to match that of W1, plus an additional increment to account for the time elapsed between the dispatch of the message by W1 and its actual delivery to W2. In general, such an increment depends on the bandwidth of the

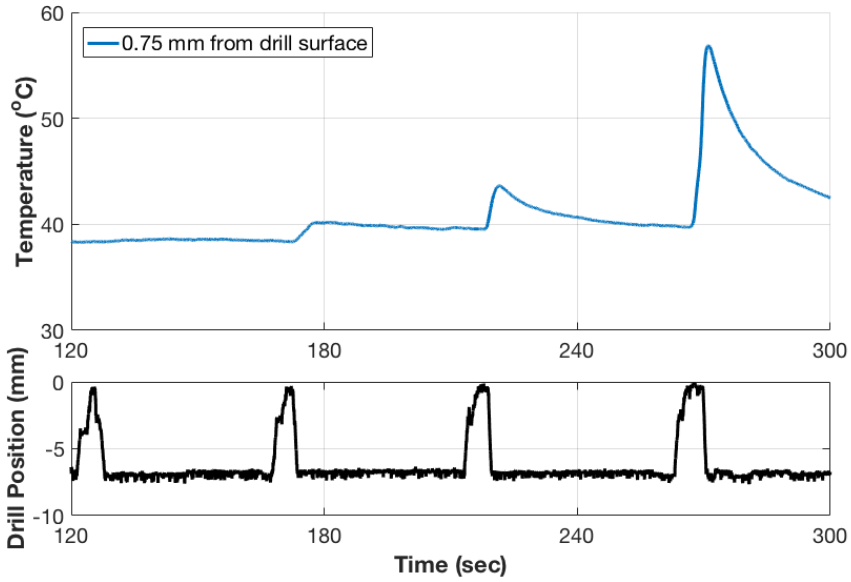

Figure 3.5: Example of synchronized thermal data and drill position advancement.

network. For simple point-to-point network configurations such as the one considered here, the communication delay is generally negligible. To verify this assumption, we estimated the time required to deliver a message from one workstation to the other as the half of the round trip time (RTT). The RTT between W1 and W2 was measured by repeatedly sending a small communication packet from W1 to W2 and measuring the time elapsed until W1 received an acknowledgment. In all trials, the observed RTT was always <= 5 ms. To ensure data consistency, the RTT was re-measured before the execution of each bone drilling trial. Figure 3.5 shows an example of thermal data correlated with drill position advancement.

Listing 3.2: MATLAB Script for Video Acquisition from the FLIR A655sc Camera

```
1 variables: T1, local clock of W1
2            T2, local clock of W2
3            RTT, round-trip time between W1 and W2
4
5 W1 sends T1 to W2
```

```
6 W2 receives T1 from W2
7 T2 <- T1 + RTT / 2
```

3.5 Discussion

In this chapter, we introduced an experimental setup to study the temperature elevation of bone during bone drilling, and developed software to collect experiment data. The software collects thermal data from an IR camera and implements a distributed clock synchronization algorithm to enable the integration of thermal data with drill position advancement. The technical contributions presented in this chapter are expected to facilitate the investigation of thermal effects of bone drilling. At the same time, the simple solutions developed here could be used to ease the integration of IR thermography in other scenarios, both medical and non-medical.

Chapter 4

THERMAL MONITORING OF VESSEL SEALING USING A MINIATURE INFRARED CAMERA

Miniature infrared cameras have recently come to market in a form factor that facilitates packaging in endoscopic or other minimally invasive surgical instruments, e.g. the tip of a laparoscope. If absolute temperature measurements can be made with these cameras, they may be useful for non-contact monitoring of electrocautery-based vessel sealing, or other thermal surgical processes like thermal ablation of tumors. As an initial step in this direction, in this Chapter we present and validate the concept of a thermal stereo-camera system, which is able to simultaneously (1) provide superficial tissue temperature estimation and (2) monitor the thermal spread created by a cautery tool.

4.1 Thermal Stereocamera System

To prove the principle of the proposed technology, we assembled the device shown in Fig. 4.1, consisting of a pair of miniature IR cameras arranged in a stereo configuration (baseline = 27 mm). The stereo camera is mounted on a passive articulated arm for easy positioning and orientation. The IR detector is the FLIR Lepton introduced in Section 2.4.2. To obtain the video stream produced by the cameras, these were mounted on two breakout

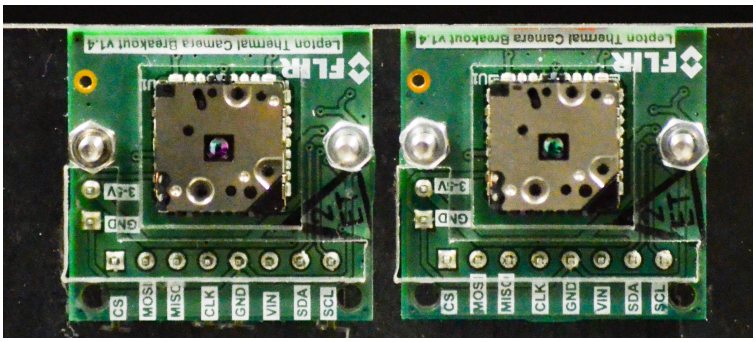

Figure 4.1: Thermal stereocamera system based on the FLIR Lepton.

boards (Pure Engineering LLC, CA) and then interfaced to a single board computer running GNU/Linux (Raspberry PI 3 Model B, Raspberry PI Foundation, UK).

As described earlier in Section 2.4.2, the FLIR Lepton does not provide absolute temperature measurements and needs to undergo a calibration procedure. We calibrated the cameras to estimate temperatures in the range between 40 and 150°C. We then performed an optical calibration of the stereo camera to enable three-dimensional (3D) scene reconstruction from the thermal images. This will enable us to monitor the spatial extent of thermal spread in the physical space, as we shall see later in Section 4.2.

4.1.1 Temperature Calibration

Infrared (IR) thermal cameras can estimate the superficial temperature of a target based on its infrared emission (recall from Section 2.1 that any object whose temperature is above absolute zero emits radiation in the IR range of wavelengths [19]). As introduced in Section 2.2, IR camera calibration typically uses a blackbody to obtain temperature reference. Industrial-grade blackbodies guarantee the best calibration results, yet these devices are not always readily available. For this study, we developed an alternative method to create controlled reference temperatures: a cylindrical block of steel (4140 alloy, radius and height are 76.2 mm and 27.9 mm respectively) was covered in high emissivity paint and heated up using a hot plate (Fig. 4.2a). The upper surface of the cylinder was used as reference for the calibration (Fig. 4.2b). The high emissivity of the paint (between 0.9 and 0.95 according to [61]) is advantageous since it provides a strong IR signal to the camera; at the same time, the thermal inertia of the steel cylinder ensures a slow variation of superficial temperature, thus providing a stable, uniform reference.

The calibration procedure consisted of exposing each of the FLIR Lepton cameras to known temperature references and calculating the best fit between pixel value and temperature. Ideally, such a process should be performed individually for each pixel [19], but for the sake of simplicity we assume that all the 60x80 = 4800 pixels present the same

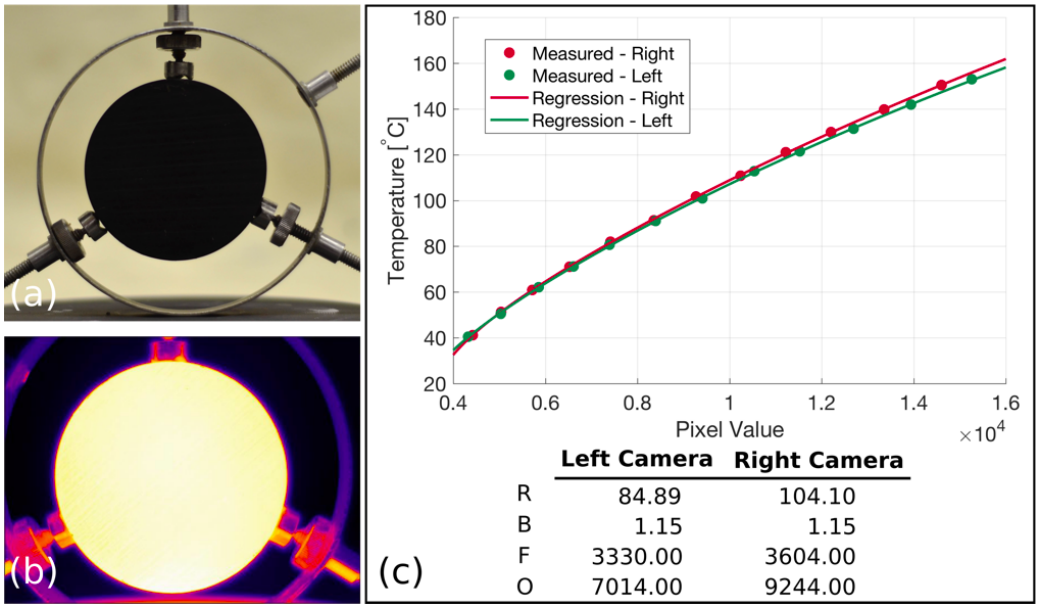

Figure 4.2: Temperature calibration: (a) steel cylinder used as temperature reference for the calibration - the upper surface was painted with charcoal grill paint to increase its emissivity; (b) thermal image of the same steel cylinder heated up at 65°C - the image was captured with a FLIR A655sc camera; (c) calibration results - the chart on the top the final calibration curves calculated for each of the two cameras, while the table below it reports the regression coefficients.

response when exposed to a given temperature reference. We acquired a total of 12 raw thermal pictures of the steel cylinder surface, taken at 10°C increments between 40 and 150°C. The mean temperature at the upper surface of the cylinder was selected as the input of our calibration model. The ground truth for the calibration was obtained by means of another, factory-calibrated, thermal camera (FLIR A655sc, FLIR Systems Inc., CA).

The relation between the camera raw output and the corresponding temperature was modeled using Eq. (2.4). The models of both cameras were estimated by nonlinear least squares regression. Results of the calibration procedure are shown in Fig. 4.2(c). The root-mean-square error (RMSE) was 0.41°C and 0.37°C for the left and right camera, respectively.

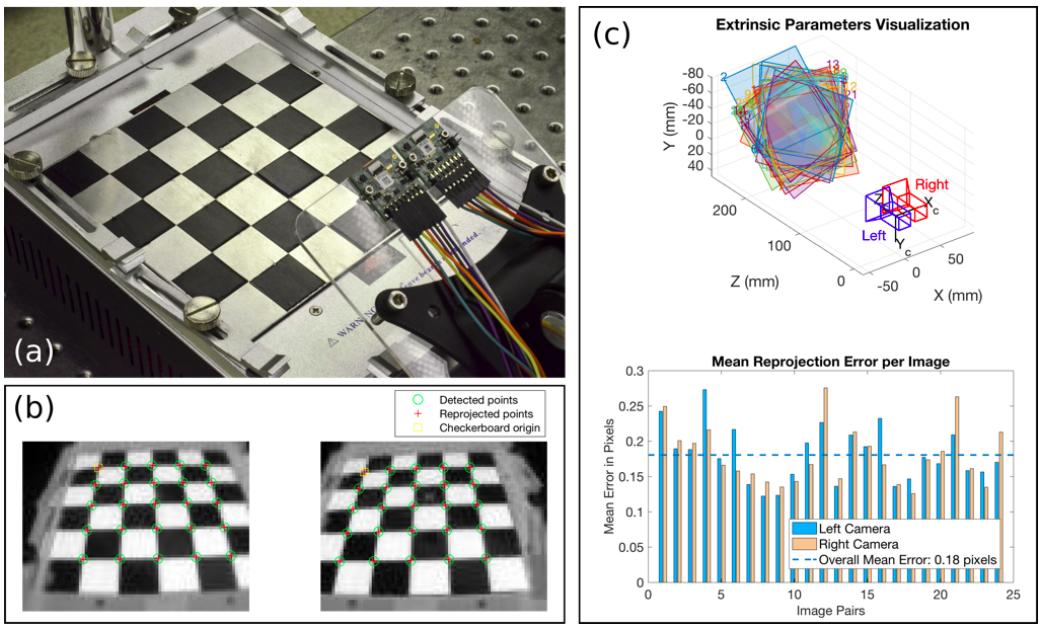

Figure 4.3: Thermal stereocamera calibration: (a) checkerboard pattern used for the calibration - black and white squares are made of materials with very different emissivity values in order to enhance the contrast in the infrared images (b) and facilitate corner detection; (c) camera-centric view of the checkerboard patterns (top) and mean reprojection error calculated on each image - a total of 24 image pairs were used in the calibration.

4.1.2 Optical Stereo Calibration

We used the MATLAB Stereo Calibration App [62] to calculate the parameters of the stereocamera, including parameters of each camera (focal length, optical center, etc.), rotation matrix and translation vector between the two cameras. The calibration used a checkerboard pattern (Fig. 4.3b), wherein the size of each square is 25 mm. The checkerboard was created out of an aluminum sheet (whose emissivity is typically quoted at $\varepsilon \approx 0.05 - 0.07$ [21]) on which black squares were made by applying electrical tape (3M Scotch Super 88 vinyl, $\varepsilon = 0.95$ [63]). The large difference between the emissivity values of these two materials enables thermal cameras to clearly see the checkerboard when this is heated up (Fig. 4.3b).

Results of the calibration process are shown in Fig. 4.3c. A total of 24 stereo image pairs were used in the calibration, with a mean reprojection error of 0.18 pixels. The calibrated stereocamera enables 3D measurements in the physical space. To validate the accuracy

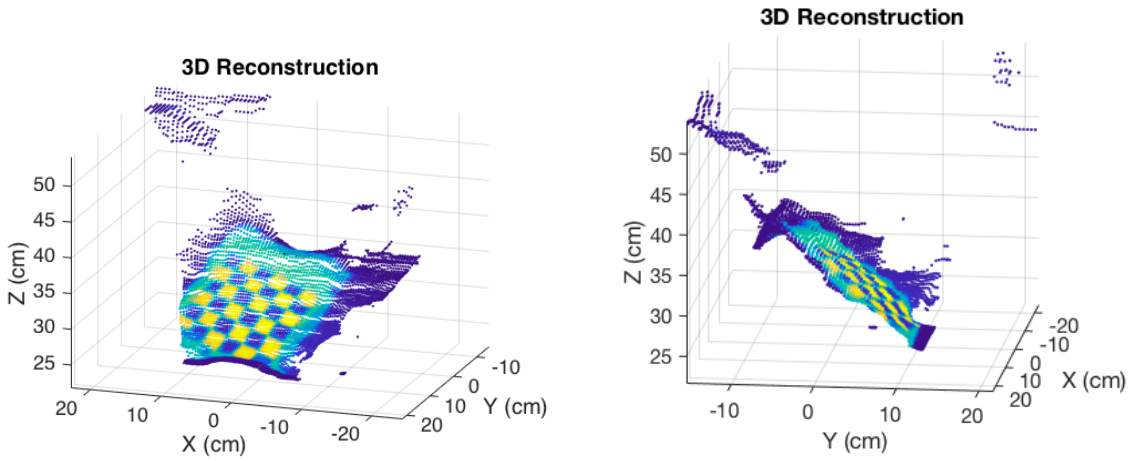

(a) 3D point cloud with the y-axis pointing towards the observer.

(b) 3D point cloud with the x-axis pointing towards the observer.

Figure 4.4: Example of 3D reconstruction of the checkerboard after stereo calibration.

of the measurements performed with this method, we implemented 3D reconstruction of the checkerboard (see Fig. 4.4) using MATLAB Computer Vision System Toolbox [64]. Bouguet's algorithm, which reprojects two-dimensional (2D) points to 3D points using parameters of the stereocamera system, was used to construct the 3D point cloud [65]. We estimated a total of 40 edges of the 16 blocks on the center of the checkerboard based on the 3D point cloud, obtaining an average length of 24.37 mm (true length: 25 mm) and a standard deviation of 2.32 mm.

4.2 Experimental Validation

Having presented both the temperature and optical calibration of the stereocamera, we now report on a benchtop experiment aimed to validating the cameras' ability to monitor the temperature of tissue. The experimental setup is shown in Fig. 4.5a. We used a disposable cautery unit (Bovie Medical Corporation, Clearwater, FL) to achieve localized coagulation on a sample of ex-vivo chicken tissue. The tip of the cautery pen (Fig. 4.5b) was put in contact with the surface of the tissue, and heat was continually applied for 10 seconds. The procedure was simultaneously recorded with the thermal stereocamera, which was posi-

tioned at a distance of 10 cm from the heat application point [1] and with a factory-calibrated thermal camera, namely the FLIR A655sc. The sequence of stereo images captured by the thermal stereocamera was processed to extract (1) the temperature readings of each camera; (2) 3D pictures (i.e. point clouds) of the tissue surface. Combining the temperature information with the point cloud produces a 3D thermal map of the tissue surface, such as the one shown in Fig. 4.5c. Such a map enables the quantitative estimation of the area of tissue subject to temperature elevation, which can be simply calculated by performing a Delaunay triangulation of the points in the map and summing up the areas of the triangles in the resulting mesh. Because the tissue surface was flat, MATLAB Statistics and Machine Learning Toolbox [66] was used to implement PCA to project the 3D thermal map to a 2D thermal map. The MATLAB Optimization Toolbox [67] was used to fit a 2D Gaussian function to the 2D thermal map and estimate the temperature spatial spreads (the average of the deviations of the 2D Gaussian function) surrounding the heat application point.

The same set of information, i.e. the temperature, area of heated tissue and temperature spatial spread, was extracted from the images collected by the FLIR A655sc and used as ground truth for the validation. Before the experiment, we positioned a ruler on the surface of tissue and took a picture of it to calculate the ratio of the pixel number to actual size. This ratio enabled spatial measurements in the FLIR A655sc images. The ruler was removed after the experiment began. Since the presence of the cautery pen in the thermal images might occlude the view of underlying tissue, the cautery tool was removed from the image immediately after heat application concluded, and then a measurements was recorded.

4.2.1 Temperature Estimation

Fig. 4.6 shows the mean and peak temperature observed in the area surrounding the heat application point. This area was segmented in the thermal images by including only those pixels for which temperature greater than or equal to 40°C. The deviation (RMSE) between

[1] minimum focusing distance quoted for the FLIR Lepton

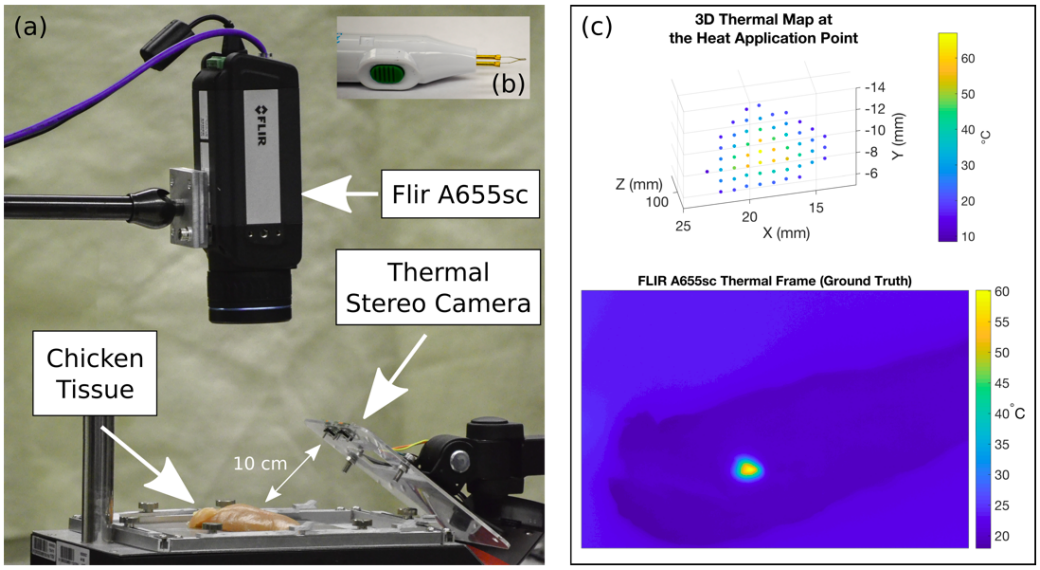

Figure 4.5: Experimental validation of the thermal stereocamera: (a) experimental setup - a disposable electrocautery pen (b) is used to achieve pinpoint coagulation on a sample of ex-vivo chicken muscle tissue; the procedure is recorded with another thermal camera (FLIR A655sc) to generate the ground truth for the validation; (c) the figure at the top shows a sample of 3D thermal image generated by the stereocamera; the bottom figure illustrates a sample of thermal image generated by the FLIR A655sc and used as ground truth in the validation process.

the ground truth mean temperature and the one detected by the FLIR Leptons was 0.76°C and 1.17°C, for the right and left camera respectively. Similarly, the RMSE between the ground truth peak temperature and the one detected by the FLIR Leptons was 3.82°C and 3.30°C. These metrics were calculated based on a total of 173 data points.

4.2.2 Spatial Extent of Thermal Spread

At each point in time, we estimated the surface area and temperature spatial spread of tissue where temperature was greater than or equal to 40°C. We found an RMSE of 12.52 mm^2 between the estimation of surface area provided by the thermal stereocamera and the output of the FLIR A655sc, and an RMSE of 0.40 mm between the temperature spatial spread estimated from the stereocamera and the FLIR A655sc. These metrics were calculated based on a total of 147 data points.

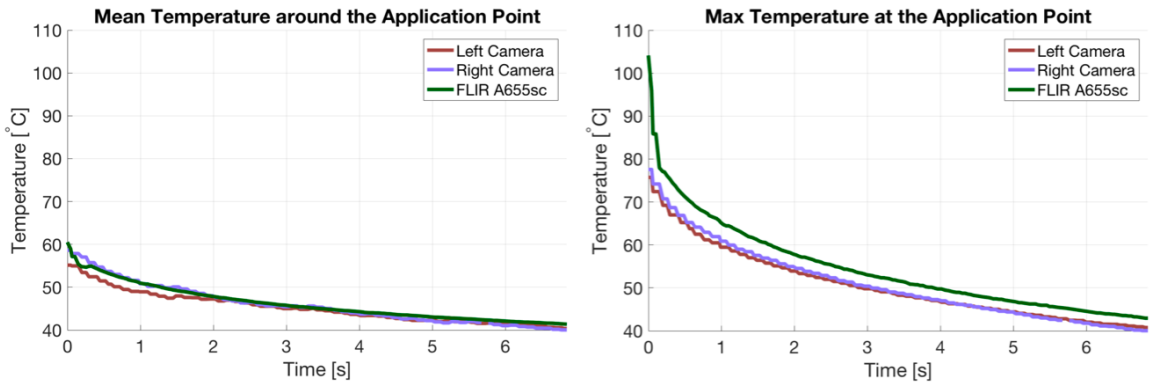

Figure 4.6: Mean and peak temperature created by the cautery pen on the surface of tissue.

4.3 Discussion

Results of the validation experiment indicate that the thermal stereocamera is capable of detecting and monitoring thermal processes on the surface of tissue. Temperature readings were found to be in line with the real tissue temperature, thereby validating the temperature calibration. Also, the estimation of the spatial extent of thermal spread is consistent with the one extracted from the FLIR A655sc; the estimation error can be explained in light of the coarser resolution of the FLIR Lepton detectors (60x80) as compared to FLIR A655sc (480x640).

One limitation of this study is that it does not quantify the accuracy of each individual stereocamera pixel. This is an important aspect, especially in light of the peak temperature estimation results (refer to the right plot in Fig. 4.6): this error was particularly large at the beginning of the experiment when the Leptons detected a peak slightly below 80 °C, but the FLIR A655sc measured a peak above 100 °C. In a first analysis, this could be explained by an incorrect temperature reading by one (or more) pixels, however we suspect this is due to the limited resolution of the FLIR Lepton IR detectors: the combination of image resolution and distance from the target gives the stereocamera a resolution of approximately 1 mm^2 on the tissue surface. Consequently any little “hot” spot ends up being averaged out by the temperature in the surroundings, resulting in an incorrect peak temperature reading. This hypothesis was corroborated by further analysis of the FLIR A655sc thermal images, which

revealed that temperature peaks were always detected in very small regions on the surface of tissue (as small as 0.03 mm^2). We verified the validity of this hypothesis by showing that the difference between the temperature spatial spread estimated from the stereo camera and the FLIR A655sc is very small. In the future, we plan to further explore this issue by comparing the temperature output of each individual stereocamera pixel with the set of measurements made by the FLIR A655sc in the surface area covered by that pixel. This analysis will require a registration method to relate pixels in the stereocamera images to pixels in the FLIR A655sc.

The study reported here represents an initial step in the creation of an IR-based surgical thermometry platform, and additional work will be required to bring the system closer to clinical use. In particular, we envision a system capable of integrating the thermal monitoring demonstrated in this Chapter with patient anatomy information derived from medical images (e.g. pre-operative CT scans), so to enable the thermal supervision of sensitive organs that could be located close to the surgical scene. We anticipate this will require a method to intraoperatively register the stereocamera images with other medical imaging modalities. To facilitate the evaluation and testing of the proposed platform, we plan to miniaturize the stereocamera design described here so that it could be scaled down onto the tip of a endoscope/laparoscope. In addition to the proposed application, in the future we expect that this platform will enable the exploration of novel applications of IR thermography in medicine.

Chapter 5

CONCLUSIONS AND FUTURE OUTLOOK

In this thesis, we presented novel technical contributions aimed to facilitate to use of IR thermography in surgical applications. These contributions include (1) a software system that acquires the video stream produced by commercial IR cameras and is capable of synchronizing the video stream with the output of other sensors that might be used in the operating room; (2) the prototype of a miniature 3D thermal camera system aimed to provide monitoring of thermal processes occurring in a surgical scenario, i.e. thermal sealing of blood vessels. This thesis represents the first study on the viability of IR-based surgical thermometry.

The work described in this thesis is expected to open up several new avenues of research. Future work will focus on translating the algorithms and systems presented here into clinical-ready technologies, so that their clinical viability could be assessed. The software presented in Chapter 3 will be extended to include a graphical user interface, in order to provide the surgeon with on-line thermal information. Another potential extension of this technology involves the use of temperature information to *close the loop* and implement automatic temperature control during the use of heat-based instruments. In its simplest formulation, the control loop could implement an emergency switch that interrupts the application of heat whenever the temperature of a critical organ (as defined by the surgeon) is about the exceed a certain threshold.

Additional work will also be focused on scaling the thermal stereocamera prototype introduced in Chapter 4 into a smaller device (e.g. a laparoscope), so that it could be easily deployed inside the body during a minimally-invasive procedure.

BIBLIOGRAPHY

[1] J. C. Lantis, F. M. Durville, R. Connolly, and S. D. Schwaitzberg. Comparison of coagulation modalities in surgery. *Journal of Laparoendoscopic & Advanced Surgical Techniques*, 8(6):381–394, 1998.

[2] M. H. Niemz. *Laser-tissue interactions: fundamentals and applications*. Springer Science & Business Media, 2007.

[3] L. J. Hefermehl, R. A. Largo, T. Hermanns, C. Poyet, T. Sulser, and D. Eberli. Lateral temperature spread of monopolar, bipolar and ultrasonic instruments for robot-assisted laparoscopic surgery. *British Journal of Urology International*, 114(2):245–252, 2014.

[4] T. E. Ahlering, D. Skarecky, and J. Borin. Impact of cautery versus cautery-free preservation of neurovascular bundles on early return of potency. *Journal of Endourology*, 20(8):586–589, 2006.

[5] D. F. Penson, D. McLerran, Z. Feng, L. Li, P. C. Albertsen, F. D. Gilliland, A. Hamilton, R. M. Hoffman, R. A. Stephenson, A. L. Potosky, et al. 5-year urinary and sexual outcomes after radical prostatectomy: results from the prostate cancer outcomes study. *The Journal of Urology*, 173(5):1701–1705, 2005.

[6] J. Wondergem, J. Haveman, V. Rusman, P. Sminia, and J. D. P. Van Dijk. Effects of local hyperthermia on the motor function of the rat sciatic nerve. *International Journal of Radiation Biology*, 53(3):429–438, 1988.

[7] M. H. Niemz. *Laser-Tissue Interactions: Fundamentals and Applications*. Springer Science & Business Media, 2013.

[8] L. Fichera. *Cognitive Supervision for Robot-Assisted Minimally Invasive Laser Surgery*. Springer Publishing Company, Incorporated, 2016.

[9] C. Song, B. Tang, P. A. Campbell, and A. Cuschieri. Thermal spread and heat absorbance differences between open and laparoscopic surgeries during energized dissections by electrosurgical instruments. *Surgical Endoscopy*, 23(11):2480–2487, 2009.

[10] J. Carlander, C. Koch, L. Brudin, C. Nordborg, O. Gimm, and K. Johansson. Heat production, nerve function, and morphology following nerve close dissection with surgical instruments. *World Journal of Surgery*, 36(6):1361–1367, 2012.

[11] E. W. Elliott-Lewis, A. M. Mason, and D. L. Barrow. Evaluation of a new bipolar coagulation forceps in a thermal damage assessment. *Neurosurgery*, 65(6):1182–1187, 2009.

[12] R. Rothmund, B. Kraemer, F. Neis, S. Brucker, M. Wallwiener, A. Reda, A. Hausch, M. Scharpf, and M. N. Szyrach. Efficacy and safety of the novel electrosurgical vessel sealing and cutting instrument BiCision®. *Surgical Endoscopy*, 26(11):3334–3343, 2012.

[13] J. Wagenpfeil, M. Jung, B. Nold, A. Neugebauer, M. Ederer, B. Krämer, R. Rothmund, C. Schwentner, D. Wallwiener, A. Stenzl, M. Schenk, M. Enderle, O. Sawodny, and R. Feuer. Optimized generator modes for bipolar vessel sealing. In *2015 IEEE Conference on Control Applications (CCA)*, pages 1862–1867, Sept 2015.

[14] P. R. Fuchshuber, T. N. Robinson, L. S. Feldman, D. B. Jones, and S. D. Schwaitzberg. The SAGES FUSE program: bridging a patient safety gap. *Bull Am Coll Surg*, 99(9):18–27, 2014.

[15] S. Braungart, C. McNaught, J. M. MacFie, and M. B. Peter. Not getting our fingers

burnt: do surgeons know enough about energy devices? *The Bulletin of the Royal College of Surgeons of England*, 98(6):244–247, 2016.

[16] P. Saccomandi, E. Schena, and S. Silvestri. Techniques for temperature monitoring during laser-induced thermotherapy: an overview. *International Journal of Hyperthermia*, 29(7):609–619, 2013.

[17] D. Pardo, L. Fichera, D. Caldwell, and L. S. Mattos. Learning temperature dynamics on agar-based phantom tissue surface during single point CO_2 laser exposure. *Neural Processing Letters*, 42(1):55–70, 2015.

[18] G. Gaussorgues and S. Chomet. *Infrared Thermography*, volume 5. Springer Science & Business Media, 2012.

[19] M. Vollmer and K. P. Möllmann. *Infrared Thermal Imaging: Fundamentals, Research and Applications*. John Wiley & Sons, 2010.

[20] M. Luciuk. Temperature and radiation. http://www.asterism.org/tutorials/tut40RadiationTutorial.pdf.

[21] FLUKE®. Emissivity values of common materials. http://support.fluke.com/find-sales/Download/Asset/3038318_6251_ENG_A_W.PDF.

[22] B. F. Jones and P. Plassmann. Digital infrared thermal imaging of human skin. *IEEE Engineering in Medicine and Biology Magazine*, 21(6):41–48, 2002.

[23] Incorporated Merriam-Webster. Room temperature. https://www.merriam-webster.com/dictionary/room+temperature.

[24] H. Budzier and G. Gerlach. Calibration of uncooled thermal infrared cameras. *Journal of Sensors and Sensor Systems*, 4(1):187–197, 2015.

[25] S. M. Bower, J. Kou, and J. R. Saylor. A method for the temperature calibration of an infrared camera using water as a radiative source. *Review of Scientific Instruments*, 80(9):095107, 2009.

[26] LumaSense^{TM} Technologies. IR calibration. https://www.lumasenseinc.com/EN/products/technology-overview/our-technologies/ircalibration/ir-calibration.html.

[27] Palmer Wahl Instrumentation Group. Black body calibration sources surface hot plate type. http://www.palmerwahl.com/product_line.php?cat=7&catl=7&line=504.

[28] R. Usamentiaga, P. Venegas, J. Guerediaga, L. Vega, J. Molleda, and F. G. Bulnes. Infrared thermography for temperature measurement and non-destructive testing. *Sensors*, 14(7):12305–12348, 2014.

[29] B. B. Lahiri, S. Bagavathiappan, T. Jayakumar, and J. Philip. Medical applications of infrared thermography: a review. *Infrared Physics & Technology*, 55(4):221–235, 2012.

[30] Y. V. Gulyaev, A. G. Markov, L. G. Koreneva, and P. V. Zakharov. Dynamical infrared thermography in humans. *IEEE Engineering in Medicine and Biology Magazine*, 14(6):766–771, 1995.

[31] P. C. Sun, H. D. Lin, S. H. E. Jao, Y. C. Ku, R. C. Chan, and C. K. Cheng. Relationship of skin temperature to sympathetic dysfunction in diabetic at-risk feet. *Diabetes research and clinical practice*, 73(1):41–46, 2006.

[32] S. Bagavathiappan, J. Philip, T. Jayakumar, B. Raj, P. N. S. Rao, M. Varalakshmi, and V. Mohan. Correlation between plantar foot temperature and diabetic neuropathy: a case study by using an infrared thermal imaging technique. *Journal of diabetes science and technology*, 4(6):1386–1392, 2010.

[33] M. Bharara, J. Schoess, and D. G. Armstrong. Coming events cast their shadows before: detecting inflammation in the acute diabetic foot and the foot in remission. *Diabetes/metabolism research and reviews*, 28(S1):15–20, 2012.

[34] B. G. Vainer. Fpa-based infrared thermography as applied to the study of cutaneous perspiration and stimulated vascular response in humans. *Physics in Medicine and biology*, 50(23):R63, 2005.

[35] R. Amalric, D. Giraud, C. Altschuler, F. Amalric, J. M. Spitalier, H. Brandone, Y. Ayme, and A. A. Gardiol. Does infrared thermography truly have a role in present-day breast cancer management? *Progress in clinical and biological research*, 107:269–278, 1981.

[36] P. Gamagami, M. J. Silverstein, and J. R. Waisman. Infra-red imaging in breast cancer. In *Engineering in Medicine and Biology Society, 1997. Proceedings of the 19th Annual International Conference of the IEEE*, volume 2, pages 677–680. IEEE, 1997.

[37] J. F. Head, F. Wang, C. A. Lipari, and R. L. Elliott. The important role of infrared imaging in breast cancer. *IEEE Engineering in Medicine and Biology Magazine*, 19(3):52–57, 2000.

[38] K. Louis, J. Walter, and M. Gautherie. Long-term assessment of breast cancer risk by thermal imaging. *Biomedical Thermology. Alan R. Liss Inc*, pages 279–301, 1982.

[39] M. Moghbel and S. Mashohor. A review of computer assisted detection/diagnosis (cad) in breast thermography for breast cancer detection. *Artificial Intelligence Review*, 39(4):305–313, 2013.

[40] R. A. Thomas, K. E. Donne, M. Clement, and M. N. Kiernan. Optimized laser application in dermatology using infrared thermography. In *AeroSense 2002*, pages 424–434. International Society for Optics and Photonics, 2002.

[41] M. Cummings, P. Biagioni, P. J. Lamey, and D. J. Burden. Thermal image analysis of electrothermal debonding of ceramic brackets: an in vitro study. *The European Journal of Orthodontics*, 21(2):111–118, 1999.

[42] F. Watanabe, Y. Tawada, S. Komatsu, and Y. Hata. Heat distribution in bone during preparation of implant sites: heat analysis by real-time thermography. *International Journal of Oral & Maxillofacial Implants*, 7(2), 1992.

[43] W. T. Chiu, P. W. Lin, H. Y. Chiou, W. S. Lee, C. N. Lee, Y. Y. Yang, H. M. Lee, M. S. Hsieh, C. J. Hu, Y. S. Ho, et al. Infrared thermography to mass-screen suspected sars patients with fever. *Asia Pacific Journal of Public Health*, 17(1):26–28, 2005.

[44] H. Nishiura and K. Kamiya. Fever screening during the influenza (H1N1-2009) pandemic at Narita International Airport, Japan. *BMC infectious diseases*, 11(1):111, 2011.

[45] D. Bitar, A. Goubar, and J. C. Desenclos. International travels and fever screening during epidemics: a literature review on the effectiveness and potential use of non-contact infrared thermometers. *Euro Surveill*, 14(6):19115, 2009.

[46] E. Y. K. Ng. Is thermal scanner losing its bite in mass screening of fever due to SARS? *Medical Physics*, 32(1):93–97, 2005.

[47] A. V. Nguyen. Comparison of 3 infrared thermal detection systems and self-report for mass fever screening. *Emerging Infectious Disease journal-CDC*, 16(11), 2010.

[48] FLIR® Systems, Inc. FLIR A655sc infrared camera. http://www.flir.com/science/display/?id=46802.

[49] SparkFun Electronics®. FLIR Dev Kit. https://www.sparkfun.com/products/13233.

[50] Automated Imaging Association (AIA). GigE Vision - true plug and play connectivity. http://www.visiononline.org/vision-standards-details.cfm?type=5.

[51] FLIR® Systems, Inc. FLIR Lepton. http://www.flir.com/cores/lepton/.

[52] J. P. Roche and M. R. Hansen. On the horizon: cochlear implant technology. *Otolaryngologic Clinics of North America*, 48(6):1097–1116, 2015.

[53] Edwtie. A internal part of a cochlear implants. https://commons.wikimedia.org/wiki/File:Cochearimplants.JPG.

[54] N. Davis. Bionic ears: let's hear it for cochlear implants. https://www.theguardian.com/science/2014/mar/16/bionic-ears-cochlear-implants-transformed-lives-children.

[55] R. F. Labadie, R. Balachandran, J. H. Noble, G. S. Blachon, J. E. Mitchell, F. A. Reda, B. M. Dawant, and J. M. Fitzpatrick. Minimally invasive image-guided cochlear implantation surgery: First report of clinical implementation. *The Laryngoscope*, 124(8):1915–1922, 2014.

[56] M. Caversaccio, K. Gavaghan, W. Wimmer, T. Williamson, J. Ansò, G. Mantokoudis, N. Gerber, C. Rathgeb, A. Feldmann, F. Wagner, et al. Robotic cochlear implantation: surgical procedure and first clinical experience. *Acta Oto-Laryngologica*, pages 1–11, 2017.

[57] N. P. Dillon, J. E. Mitchell, M. G. Zuniga, R. J. Webster, and R. F. Labadie. Design and thermal testing of an automatic drill guide for less invasive cochlear implantation. *Journal of Medical Devices*, 10(2):020923, 2016.

[58] A. Feldmann and P. Zysset. Experimental determination of the emissivity of bone. *Medical engineering & physics*, 38(10):1136–1138, 2016.

[59] MathWorks. Image Acquisition Toolbox. https://www.mathworks.com/help/imaq/index.html.

[60] F. Cristian. Probabilistic clock synchronization. *Distributed computing*, 3(3):146–158, 1989.

[61] FLIR® Systems, Inc. Use low-cost materials to increase target emissivity. http://www.flir.com/science/blog/details/?ID=71556.

[62] MathWorks. Stereo Calibration App. https://www.mathworks.com/help/vision/ug/stereo-camera-calibrator-app.html.

[63] R. P. Madding. Emissivity measurement and temperature correction accuracy considerations. volume 3700, pages 393–401, 1999.

[64] MathWorks. Computer Vision System Toolbox. https://www.mathworks.com/help/vision/index.html.

[65] Gary Bradski and Adrian Kaehler. *Learning OpenCV: Computer vision with the OpenCV library*. " O'Reilly Media, Inc.", 2008.

[66] MathWorks. Statistics and Machine Learning Toolbox. https://www.mathworks.com/help/stats/index.html.

[67] MathWorks. Optimization Toolbox. https://www.mathworks.com/help/optim/index.html.